Front. Earth Sci. 2020, 14(1): 171–187
https://doi.org/10.1007/s11707-019-0770-z

RESEARCH ARTICLE

Scale problem: Influence of grid spacing of digital elevation model on computed slope and shielded extra-terrestrial solar radiation

Nan CHEN (✉)[1,2]

1 Key Laboratory of Spatial Data Mining & Information Sharing (Ministry of Education), Fuzhou University, Fuzhou 350108 China
2 Spatial Information Research Center of Fujian Province, Fuzhou University, Fuzhou 350108 China

© Higher Education Press and Springer-Verlag GmbH Germany, part of Springer Nature 2019

Abstract Solar radiation is the primary energy source that drives many of Earth's physical and biological processes and determines the patterns of climate and productivity on the surface of the Earth. A fundamental proportion of solar radiation is composed of shielded extra-terrestrial solar radiation (SESR), which can be computed using the slope and aspect derived from a digital elevation model (DEM). The objective of this paper is to determine the influence of the grid spacing of the DEM (the influence of the scale of the DEM) on the errors of slope, aspect and SESR. This paper puts forward the concepts of slope representation error, aspect representation error, and SESR representation error and then studies the relations among these errors and the grid spacing of DEMs. We find that when the grid spacing of a DEM becomes coarser, the average SESR increases; the increase in SESR is dominated by the grid cells of the DEM with a negative slope representation error, whereas SESR generally decreases in the grid cells with a positive slope representation error. Although the grid spacing varies, the distribution of the percentages of positive SESR representation errors on the slope, which is classified into 11 slope intervals, is independent of the grid spacing; this distribution is concentrated across some slope intervals. Moreover, the average absolute value and mean square error of the SESR representation error are closely related to those of the slope representation error and the aspect representation error. The findings in this study may be useful for predicting and reducing the errors in SESR measurements and may help to avoid mistakes in future research and in practical applications in which SESR is the data of interest or plays a vital role in an analysis.

Received September 25, 2018; accepted May 29, 2019

E-mails: chennan@fzu.edu.cn; fjcn99@163.com

Keywords scale problem, digital elevation model, grid spacing, slope, shielded extra-terrestrial solar radiation

1 Introduction

"Solar radiation is the ultimate energy source of the terrestrial system" (Liu et al., 2012) because it plays important roles in meteorological (Pellicciotti et al., 2011), hydrological (Hopkinson et al., 2010) and biological processes (Häntzschel et al., 2005; Piedallu and Gégout, 2008). "Solar radiation changes the distribution of clouds, temperature, moisture, and precipitation as well as the patterns of atmospheric circulation" (Qiu et al., 2004) (i.e., solar radiation "assumes spatial heterogeneity" (Zhang et al., 2015)). Therefore, solar radiation has been extensively studied by scientists in many fields, such as vegetation modeling (Piedallu and Gégout, 2007), solar electricity generation (Šúri et al., 2007), and climate simulation (Yao et al., 2011).

The solar radiation reaching a plot of land is influenced by the atmosphere and terrain relief. "When solar radiation traverses the Earth's atmosphere, it is attenuated by various atmospheric constituents, such as ozone, oxygen, carbon dioxide, moisture, water droplets, and clouds; solar radiation reaching the top of the atmosphere is called extra-terrestrial solar radiation (ESR) or astronomical solar radiation" (Huang et al., 1986). On the other hand, the ESR reaching a plot is shielded by the terrain relief around the plot; shielded ESR is called SESR in this paper.

SESR is the fundamental data through which scientists compute the direct, diffusive, and global solar radiation intensities when required meteorological parameters are known (e.g., the atmospheric transparency, cloud cover, and temperature) (Wang et al., 2014; Zhang et al., 2017). In addition, "SESR is a vital astronomical parameter for

evaluating solar energy resources and agricultural production potential" (Zuo, 1990; Qiu et al., 2005), but solar radiation, including SESR, is difficult to measure in plots (Piedallu and Gégout, 2008).

Methods for computing the SESR have gained attention. Initially, SESR has been directly computed using theoretical formulas when the latitude, solar declination, and solar hour angle are known (Huang et al., 1986; Li et al., 1999) without considering the shielding caused by relief. Currently, shielding on Earth, especially on rugged terrains, is considered, and thus, theoretical formulas for computing the SESR have been developed (Li and Weng, 1988; Dozier and Frew, 1990; Bocquet, 2010; Zhang et al., 2015). In particular, digital elevation models (DEMs) have been used to rapidly compute SESR (Dozier and Frew, 1990) over large areas because they can be used to easily derive the slope and aspect, which are two variables that are required for computing the SESR (the other two required variables are latitude and solar declination).

With the development of formulas for computing the SESR, many studies have revealed that SESR or solar radiation is strongly affected by topographic factors (Qiu et al., 2004; Reuter et al., 2005; Ambreen et al., 2011; Zhang et al., 2013). Of the topographic factors, slope has a positive relation with solar radiation, and the southern aspect generally receives more solar radiation than the northern aspect when slope is given (Zhang et al., 2010); slope and aspect influence the distribution of SESR on rugged terrains in a seasonal manner (Zeng et al., 2005). Thus, both slope and aspect are closely related to SESR.

When slope and aspect are computed by the elevations of sample points in DEMs, the elevation errors are propagated through to slope and aspect errors (Zhou and Liu, 2004), respectively, which are propagated through to solar radiation errors (Piedallu and Gégout, 2008). The elevation errors may be divided into two categories: "the terrain representation error" (Tang et al., 2001) and the elevation sample error.

• The elevation sample error has been thoroughly studied, and the methods for computing and reducing these errors are efficient, resulting in efficiently computing and reducing the slope and aspect errors (Zhou and Liu, 2004 and 2008; Chow and Hodgson, 2009; Gao et al., 2012; Chen et al., 2014; C. Li et al., 2018a and 2018b). Thus, the elevation sample error is not studied in this paper.

• The terrain representation error present by assuming that the elevation sample error is zero is unavoidable (Tang et al., 2001). Similarly, based on the terrain representation error, we may define two concepts caused by grid spacing: the slope representation error (see Fig. 1) and the aspect representation error. The two errors cannot be avoided because grid spacings cannot be infinitely fine in practice.

Therefore, how the slope and aspect representation errors change with the grid spacing of DEMs and how they propagate through to the SESR representation error (see Fig. 1) have remained unclear and may be an impediment in relevant academic fields. A lack of knowledge concerning the impediment may lead to incorrect conclusions in research in which the SESR is used as background data (e.g., the biological cycle and distribution of solar energy on Earth); a decision maker may make incorrect decisions when developing and using solar energy. Thus, the bottleneck has been discussed in our research. Our research lies in the scale problem (the variations in the grid spacing of DEMs, i.e., the variations in the scale of DEMs causes the slope representation error); our research is different from the existing research in that our research concentrates not on the error models but on the difference between the data computed by test DEMs and that of the 5 m DEM.

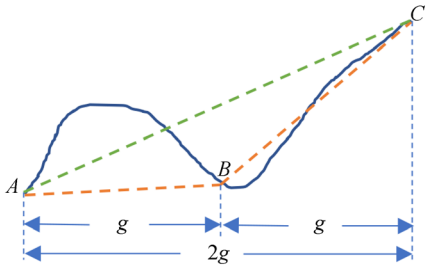

Fig. 1 Slope change caused by the change in the grid spacing of the digital elevation model. For convenience of explanation, we give a profile of the land surface, $\overset{\frown}{ABC}$, in the figure.

1) When the grid spacing is g, the slope of the curve $\overset{\frown}{AB}$ is represented by the slope computed by the elevations of the sample points A and B—the computed slope is the slope of the red dotted line segment AB. Meanwhile, the slope of the curve $\overset{\frown}{BC}$ is represented by that of the red dotted line segment BC. 2) When the grid spacing increases to $2g$, the slope of $\overset{\frown}{ABC}$ is represented by that of the green dotted line segment AC. Then, the slope of AB increases to that of AC; the corresponding increase is defined as the slope representation error for the land surface represented by AB. Similarly, the slope of BC decreases to that of AC; the corresponding decrease is defined as the slope representation error for the land surface represented by BC. 3) Moreover, based on the slope and aspect of AB, we may compute the shielded extra-terrestrial solar radiation (SESR); based on the slope and aspect of AC, we may compute the SESR. The second SESR minus the first SESR is the SESR representation error defined in this paper for the land surface represented by AB. 4) Note that the average slope generally decreases when the grid spacing increases (Jay Gao, 1997; Chow and Hodgson, 2009), whereas the slopes of some land surfaces increase (the slope of AB increases to that of AC, as shown in this figure). The reason behind the increase in slopes is discussed in this paper.

The aim of this paper is to discover how the slope, aspect and SESR representation errors of grid cells change with the grid spacing of DEMs. We find significant linear relations between the absolute average value and the mean square error of SESR representation error and those of slope representation error (or those of aspect representation

error).

The results of this paper may be beneficial to research in improving the accuracy of solar radiation data. The linear relations found in this paper may help us predict and reduce the SESR error and understand the influence of topographic relief on SESR. The concepts of the slope, aspect and SESR representation errors might be used as the accuracy indexes in the research on solar radiation and terrain relief.

2 Methods

2.1 Materials

Introduction of the sample and test areas. We chose six sample areas that represent different landforms (see Table 1). The shade relief maps of the sample areas are illustrated in Fig. 2. The six sample areas cover latitudes from 24°39′30″ to 38°52′30″N (see the average latitudes in Table 1). The corresponding average latitude in Table 1 is used as φ for computing U, V, and W in Eq. (1). In addition, we choose a test area representing hills and low- and medium-sized mountains to verify the equations for estimating the error in the SESR (see Eqs. (5), (6), (7) and (8), which are obtained in the sample areas). The test area covers latitudes from 27°7′30″N to 27°12′29″N and longitudes from 117°48′45″E to 117°56′15″E. The average latitude of the test area is approximately 27°10′00″N and is used as φ in Eq. (1).

DEMs of the sample and test areas. In the sample and test areas, the 5 m grid spacing DEMs were established from 1:10000 scale topographical maps provided by the State Bureau of Surveying and Mapping from China. 5 m grid spacing DEMs can reliably describe the terrain (Tang et al., 2001) and are assumed to represent actual terrains.

All of the DEMs above are used to compute the SESR and the possible sunshine duration (PSD), which is a vital parameter in computing the SESR and is discussed in Section 3.2 in detail, on the four typical days (Huang et al., 1986), including the vernal equinox, summer solstice, autumnal equinox and winter solstice. The four days have corresponding D_n values (see D_n in Eq. (2)) of 80, 173, 266 and 356, respectively.

2.2 Method for computing the ESR

The ESR on a slope surface is computed by Eq. (1) (Li et al., 1999).

$$I_{\alpha\beta} = (1/\rho^2)I_0(U\sin\delta + V\cos\delta\cos\omega + W\cos\delta\sin\omega), \quad (1)$$

where $I_{\alpha\beta}$ represents the ESR (in $\mathrm{MJ\cdot m^{-2}\cdot min^{-1}}$) on the slope surface, $1/\rho^2$ represents the Sun-Earth distance correction factor, I_0 represents the solar constant (0.082 $\mathrm{MJ\cdot m^{-2}\cdot min^{-1}}$), δ represents the solar declination and ω represents the solar hour angle; $U = \sin\varphi\cos\alpha - \cos\varphi\sin\alpha\cos\beta$, $V = \sin\varphi\sin\alpha\cos\beta + \cos\varphi\cos\alpha$ and $W = \sin\alpha\sin\beta$ (φ represents the latitude at the surface, α represents the slope of the surface, and β represents the aspect of the surface). Moreover, δ and $1/\rho^2$ in Eq. (1) are computed by the following Fourier series (Zuo et al., 1991).

$$\delta = 0.006894 - 0.399512\cos\tau + 0.07207\sin\tau - 0.006799\cos(2\tau) + 0.00089\sin(2\tau) - 0.002689\cos(3\tau) + 0.001516\sin(3\tau)$$

and

$$1/\rho^2 = 1.000109 + 0.033494\cos\tau + 0.001472\sin\tau + 0.000768\cos(2\tau) + 0.000079\sin(2\tau),$$

where τ represents the day angle (in radians) and is defined by Eq. (2).

$$\tau = 2\pi(D_n - 1)/365 \ (D_n = 1, 2, 3, ..., 365), \quad (2)$$

where D_n represents the ordinal number of the day of the year (e.g., $D_n = 2$ for 2 January).

By integrating $I_{\alpha\beta}$ in Eq. (1) for the PSD, we obtain the ESR that hits the surface, which is denoted by W_s in Eq. (3) (Li et al., 1999).

Table 1 The locations and landforms of the sample areas

Sample area	Longitude and latitude at the upper left corner of the sample area	Longitude and latitude at the bottom right corner of the sample area	Average latitude of the sample area	Landform
Shenmu	110°15′00″E, 38°55′00″N	110°22′30″E, 38°50′00″N	38°52′30″N	Desert and loess
Yanchuan	109°52′30”E, 36°47′30″N	110°00′00”E, 36°42′30”N	36°44′30″N	Low- and medium-sized mountains
Yijun	109°18′45″E, 35°30′00″N	109°26′15″E, 35°25′00″N	35°27′30″N	Loess ridge
Nanping	118°33′45″E, 27°52′30″N	118°41′15″E, 27°47′30″N	27°49′30″N	Hills and low- and medium-sized mountains
Sanming	117°18′45″E, 26°22′30″N	117°26′15″E, 26°17′30″N	26°19′30″N	Low- to medium-sized mountains
Zhangzhou	117°33′45″E, 24°42′30″N	117°41′15″E, 24°37′30″N	24°39′30″N	Plains

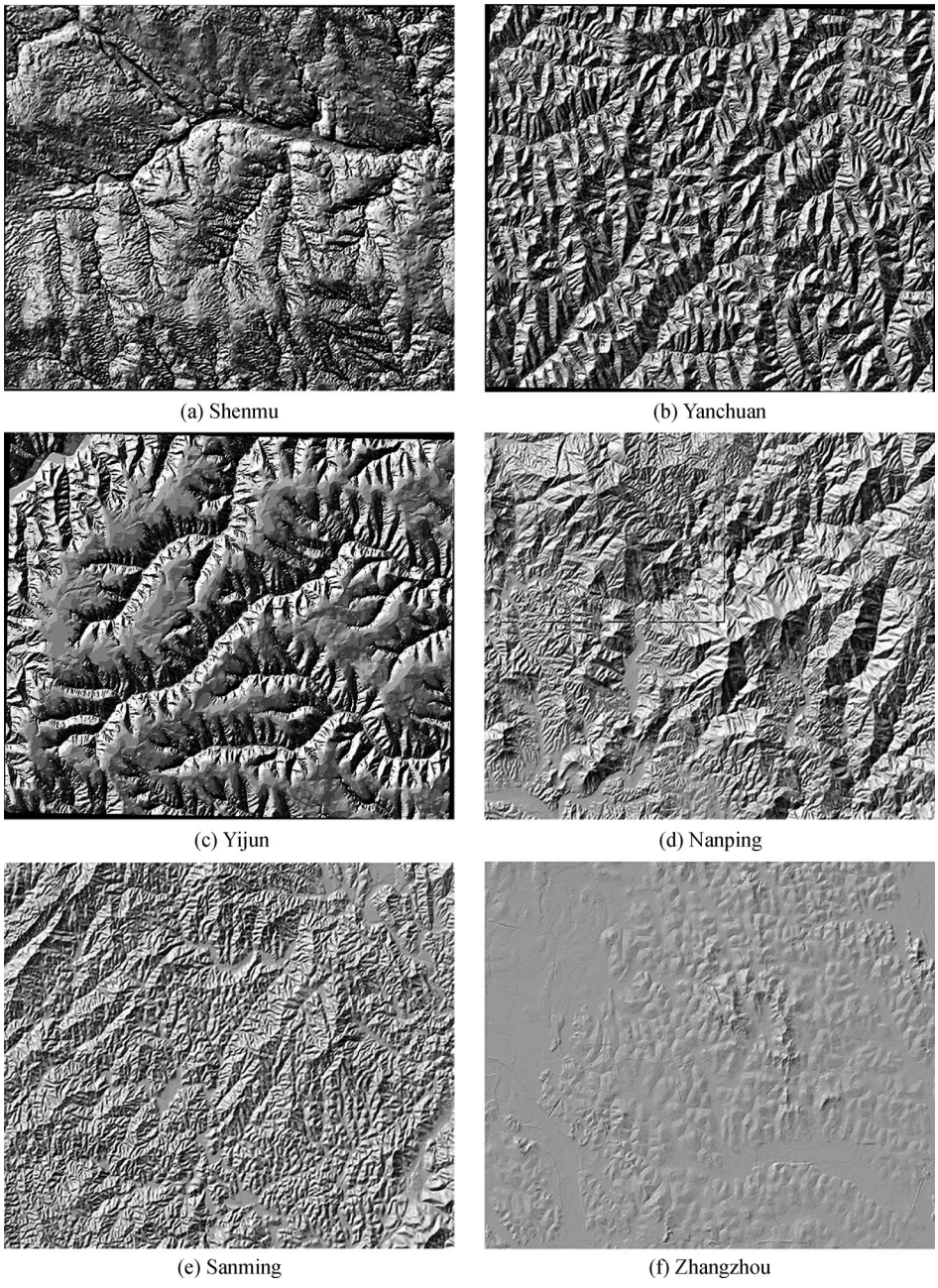

Fig. 2 Shade relief maps of the six sample areas.

$$W_s = \frac{T}{2\pi}\left(\frac{1}{\rho^2}\right) I_0 \int_{\omega_{sr}}^{\omega_{ss}} (U\sin\delta + V\cos\delta\cos\omega + W\cos\delta\sin\omega)\mathrm{d}\omega$$

$$= \frac{T}{2\pi}\left(\frac{1}{\rho^2}\right) I_0 [U\sin\delta(\omega_{ss} - \omega_{sr}) + V\cos\delta(\sin\omega_{ss} - \sin\omega_{sr}) - \sin\alpha\sin\beta\cos\delta(\cos\omega_{ss} - \cos\omega_{sr})], \quad (3)$$

where ω_{sr} (in radians) represents the solar hour angle at the beginning of the PSD, ω_{ss} (in radians) represents the solar hour angle at the end of the PSD, and T represents the total duration of one day (i.e., 1440 min).

Note that $\omega_{sr} = -\omega_{ss}$. Then, we let $\omega_{ss} = \omega_0$ and $\omega_{sr} = -\omega_0$ for convenience. ω_0 (in radians) is computed by $\omega_0 = \arccos(-\tan\delta\tan\varphi)$. $[-\omega_0, \omega_0]$ denotes the period of daily PSD from sunrise to sunset at a land point. If $[-\omega_0, \omega_0]$ is divided into several subperiods, in some subperiods, the sunshine at the point may be shielded by the relief around the point; therefore, the PSDs of the subperiods should not be considered when computing the

SESR at that point. However, $[-\omega_0, \omega_0]$ (or $[\omega_{sr}, \omega_{ss}]$) represents the interval in which W_s is integrated in Eq. (3) and, thus, W_s is computed without considering shielding in Eq. (3). Thus, Eq. (3) should be reconstructed. A reconstructed Eq. (3) is described in Section 2.3.

2.3 Method for computing the SESR

A distributed model (Qiu et al., 2005), which is a reconstructed version of Eq. (3), is as follows.

1) Divide $[-\omega_0, \omega_0]$ into subperiods and determine the subperiods available for the PSD in a DEM grid cell.

The period $[-\omega_0, \omega_0]$ may be evenly divided into N subperiods. Each subperiod has a length of $\Delta\omega$ ($\Delta\omega = 2\omega_0/N$, in radians). $\Delta\omega$ has a corresponding time step length, denoted by ΔT (in minutes), which is defined by $\Delta T = (2\omega_0/(2\pi N)) \times 24 \times 60$. ΔT should be less than 20 min (Li and Weng, 1988). Thus, N can be defined by the following equation: $N = \text{int}\left(\frac{2\omega_0}{2\pi} \times \frac{24 \times 60}{20}\right) + 1$, where int( ) is a function that obtains the integer part of the value in parenthesis. Therefore, N subperiods may be $[-\omega_0, -\omega_0 + \Delta\omega]$, $[-\omega_0 + \Delta\omega, -\omega_0 + 2\Delta\omega]$, ..., $[-\omega_0 + (N-1)\Delta\omega, \omega_0]$. Then, the ith subperiod is $[-\omega_0 + i\cdot\Delta\omega, -\omega_0 + (i+1)\cdot\Delta\omega]$, whose beginning solar hour angle is denoted by ω_i ($\omega_i = -\omega_0 + i\cdot\omega$), where $i = 0, 1, 2, ..., N-1$.

The sun elevation angle corresponding to the solar hour angle ω_i, denoted by h_i, is computed by the equation $h_i = \arcsin(\sin\delta\sin\varphi + \cos\delta\cos\varphi\cos\omega_i)$. The sun elevation angles corresponding to solar hour angles $\omega_0, \omega_1, \omega_2, ..., \omega_i, ..., \omega_N$ are denoted by $h_0, h_1, h_2, ..., h_i, ..., h_N$, respectively.

The azimuth angle corresponding to the hour angle ω_i, denoted by ϕ_i, is computed by the equation $\phi_i = \arccos[(\sin h_i \sin\varphi - \sin\delta)/(\cos h_i \cos\varphi)]$. The azimuth angles corresponding to the solar hour angles $\omega_0, \omega_1, \omega_2, ..., \omega_i, ..., \omega_N$ are denoted by $\phi_0, \phi_1, \phi_2, ..., \phi_i, ..., \phi_N$, respectively.

We now compute the shielding status within a DEM grid at a time corresponding to the solar hour angle ω_i. The shielding status within the grid cell (a grid cell is called a grid hereafter for brevity) is determined by the sun azimuth angle ϕ_i corresponding to ω_i and the surrounding relief in the direction of ϕ_i. The shielding status is described by the shielding coefficient, denoted by S_i, where $S_i = 0$ implies that shielding occurs in the direction of φ_i and $S_i = 1$ implies that shielding is unavailable. The computation of the shielding coefficients is illustrated in Fig. 3. Then, the shielding coefficients of the grid corresponding to the solar hour angles $\omega_0, \omega_1, \omega_2, .., \omega_N$ are denoted by $S_0, S_1, S_2, ..., S_N$, respectively. Thus, the average shielding coefficients $S_0, S_1, S_2, ..., S_N$ range from 0 to 1, with a higher average representing more sunshine received by the grid.

From the values of both S_i and S_{i+1}, we can decide whether sunshine is available in the corresponding subperiod $[\omega_i, \omega_{i+1}]$ (Li and Weng, 1988). If the subperiod $[\omega_i, \omega_{i+1}]$ has available sunshine (i.e., is available for the PSD), it is recorded by a subperiod $[\omega_{srl}, \omega_{ssl}]$, where ω_{srl} is equal to ω_i, and ω_{ssl} is equal to ω_{i+1}. More generally, all of the solar angle subperiods available for the PSD are recorded by $[\omega_{sr1}, \omega_{ss1}]$, $[\omega_{sr2}, \omega_{ss2}]$, ..., $[\omega_{srl}, \omega_{ssl}]$, ..., $[\omega_{srm}, \omega_{ssm}]$, where m represents the number of total solar angle periods available for the PSD (see (Qiu et al., 2005) for more details on computing the PSD).

Hereafter, the PSD of a grid implies the sum of the corresponding PSDs of the grid in the subperiods, including $[\omega_{sr1}, \omega_{ss1}]$, $[\omega_{sr2}, \omega_{ss2}]$, ..., $[\omega_{srl}, \omega_{ssl}]$, ..., $[\omega_{srm}, \omega_{ssm}]$.

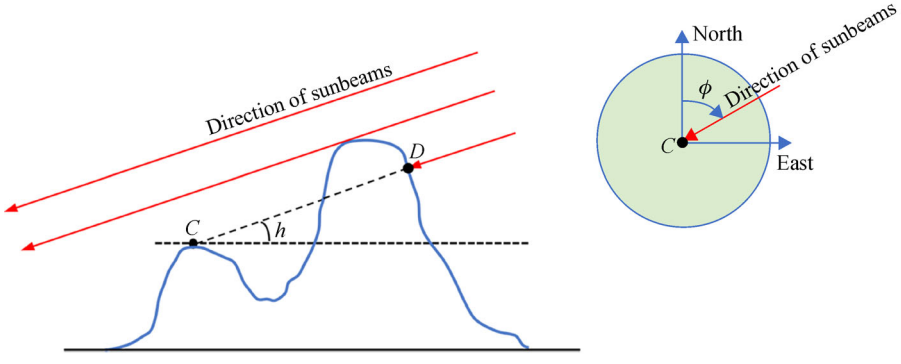

Fig. 3 Computation of the shielded coefficients. For convenience of explanation, we give a profile of the land surface (the blue curve in the figure). The red lines with arrows represent the directions of sunbeams, whose elevation angle is denoted by h (in the figure on the left) and whose azimuth angle is denoted by ϕ (in the figure on the right figure).
C and D represent points on the surface. By h and ϕ, we can determine the direction of sunbeams. Then, by the direction and the elevations around C, we can determine whether C receives sunbeams (i.e., whether shield occurs at C). At C, shielding occurs (see the left figure), and its shielding coefficient is equal to zero, whereas at D, shielding does not occur, and its shielding coefficient is equal to one. More details of computing the shielded coefficients may be referred to in (Zeng et al., 2003) and (Qiu et al., 2005).

2) Computing the daily SESR

The SESR in $[\omega_{srl}, \omega_{ssl}]$ can be computed by Eq. (3) if $[\omega_{srl}, \omega_{ssl}]$ is the integration interval of the integral in Eq. (3) instead of $[\omega_{sr}, \omega_{ss}]$. In a similar manner, the SESR values of the subperiods $[\omega_{sr1}, \omega_{ss1}]$, $[\omega_{sr2}, \omega_{ss2}]$, ..., $[\omega_{srl}, \omega_{ssl}]$, ..., $[\omega_{srm}, \omega_{ssm}]$ can be computed. Then, the computed SESR values can be summed to yield the daily SESR, denoted by $W_{0\alpha\beta}$ (in $\mathrm{MJ\cdot m^{-2}}$), which takes the form of Eq. (4).

$$W_{0\alpha\beta} = \frac{I_0 T}{2\pi}\left(\frac{1}{\rho^2}\right)\left\{U\sin\delta\sum_{l=1}^{m}(\omega_{ssl}-\omega_{srl}) + V\cos\delta\sum_{l=1}^{m}(\sin\omega_{ssl}-\sin\omega_{srl}) - W\cos\delta\sum_{l=1}^{m}(\cos\omega_{ssl}-\cos\omega_{srl})\right\}. \quad (4)$$

2.4 Method for deriving the slope and aspect from DEMs

According to Eq. (1), computing the SESR requires the slope and aspect, which are generally derived from gridded DEMs. If a terrain surface is described by the continuous function $z = f(x, y)$, we compute the slope and aspect with the equations $\text{slope} = \arctan\sqrt{f_x^2 + f_y^2}$ and $aspect = \pi - \arctan f_y/f_x + \frac{\pi}{2}\times f_x/|f_x|$, respectively. In this paper, f_x and f_y are computed using the third-order finite difference algorithm weighted by the reciprocal of the squared distance (Horn, 1981) as follows: $f_x = (z_7 - z_1 + 2(z_8 - z_2) + z_9 - z_3)/(8g)$ and $f_y = (z_3 - z_1 + 2(z_6 - z_4) + z_9 - z_7)/(8g)$. In the two equations above, z_j $(j = 1, 2, 3, ..., 9)$ denotes the elevation of the grid numbered j in Fig. 4, and g denotes the grid spacing of the DEM in Fig. 4.

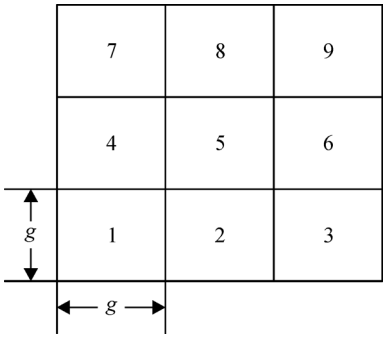

Fig. 4 A 3 × 3 gridded digital elevation model. The elevations of grid cells 1 through 9 are necessary for computing the slope (or the aspect) of grid cell 5. In this figure, g denotes the grid spacing of the digital elevation model.

2.5 Definition of error indexes

Let the slope, aspect, and SESR derived or computed using a i m grid spacing DEM be denoted by Slope_i, Aspect_i and $SESR_i$ $(i = 5, 10, 15, ..., 100$ m), respectively.

The method for deriving the slope from a 5 m (or 10 m) grid spacing DEM is illustrated in Fig. 5; the method for computing the slope representation error of grid A is illustrated in Fig. 5. We may compute the slope representation error of a grid numbered j in a 5 m grid spacing DEM by $\text{Slope}_{i,j}\_RE = \text{Slope}_{i,j} - \text{Slope}_{5,j}$, where j denotes the number of grids $(j = 1, 2, 3, ..., n)$, and n denotes the total number of grids in the DEM). We compute the average absolute value of $\text{Slope}_{i,j}\_RE$ by $\text{Slope}_i\_AA = \sum_{j=1}^{n}|\text{Slope}_{i,j} - \text{Slope}_{5,j}|/n$; Slope_i_AA takes its origin from the absolute error, which was used by (Li et al., 2018a and 2018b). We compute the mean square error (MSE) of $\text{Slope}_{i,j}\_RE$ by $\text{Slope}_i\_MSE = \sqrt{\sum_{j=1}^{n}(\text{Slope}_{i,j} - \text{Slope}_{5,j})^2/n}$; Slope_i_MSE takes its origin from the MSE, which was used by (Zhou and Liu, 2002, 2004 and 2008). Similarly, we may define $SESR_i\_RE$, $SESR_i\_AA$ and $SESR_i\_MSE$.

Because "the aspect is a circular variable" (Ruiz-Arias et al., 2009) (e.g., the aspects of 2π and 0 are the same as the northern aspect), we have to compute the aspect representation error of Aspect_i by $\text{Aspect}_{i,j}\_RE = \cos(\text{Aspect}_{i,j}) - \cos(\text{Aspect}_{5,j})$. Then, we compute the average absolute value and the MSE of Aspect_i_RE by $\text{Aspect}_i\_AA = \sum_{j=1}^{n}|\cos(\text{Aspect}_{i,j}) - \cos(\text{Aspect}_{5,j})|/n$,

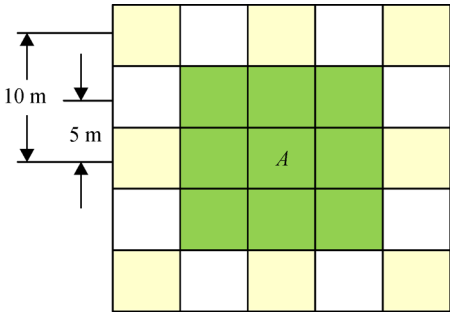

Fig. 5 Sketch map of the derivation of the slope of grid cell A from 5 m grid spacing or 10 m grid spacing digital elevation model (DEM) using the third-order finite difference algorithm weighted by the reciprocal of the squared distance. When we derive the slope of A using a 5 m grid spacing DEM, the elevations of the green grid cells are required—the derived slope is denoted by $\text{Slope}_{5,A}$; when we derive the slope of A using a 10 m grid spacing DEM, the elevations of the yellow grid cells and grid cell A are required—the derived slope is denoted by $\text{Slope}_{10,A}$. The difference, $\text{Slope}_{10,A} - \text{Slope}_{5,A}$, is the slope representation error of A.

and

$$\text{Aspect}_i\_MSE = \sqrt{\sum_{j=1}^{n} [\cos(\text{Aspect}_{i,j}) - \cos(\text{Aspect}_{5,j})]^2 / n},$$

respectively.

3 Results and discussion

3.1 Change in positive, negative, or zero Slope_*RE* with grid spacing of the DEM

For convenience of discussion, Slope_*RE* is divided into three classes by their signs: positive, negative, and zero. We find Result 1 and Result 2.

Result 1. When the grid spacing of a DEM becomes coarser, the percentage of grids with a negative Slope_*RE* is greater than that of grids with a positive Slope_*RE*; the ratio of the first percentage to the second percentage increases with the grid spacing.

Result 2. When the grid spacing of a DEM becomes coarser, the average decrease in the slope of grids with a negative Slope_*RE* is greater than the average increase in the slope of grids with a positive Slope_*RE*; the ratio of the first average to the second average increases with the grid spacing.

Result 1 and Result 2 are explained by Fig. 6. Result 1 reveals that the grids with a positive Slope_*RE*, whose percentage cannot be ignored compared with those of the grids with a negative Slope_*RE*, may exert an influence on the average slope when the grid spacing changes. The influence could be explained by Result 2.

By combining Result 1 and Result 2, we may more deeply understand the fact that the average slope decreases with grid spacing (Gao, 1997; Chow and Hodgson, 2009). Result 1 states that the grids with a negative Slope_*RE* comprise the majority of grids and increase with grid spacing; Result 2 states that these grids dominate the decrease in slope and contribute a greater decrease in slope when the grid spacing becomes coarser. Together, the grids with a negative Slope_*RE* may dominate the change in slope when the grid spacing becomes coarser. Then, the slope generally decreases (i.e., the represented relief reduces) and, thus, the average slope decreases when the grid spacing becomes coarser.

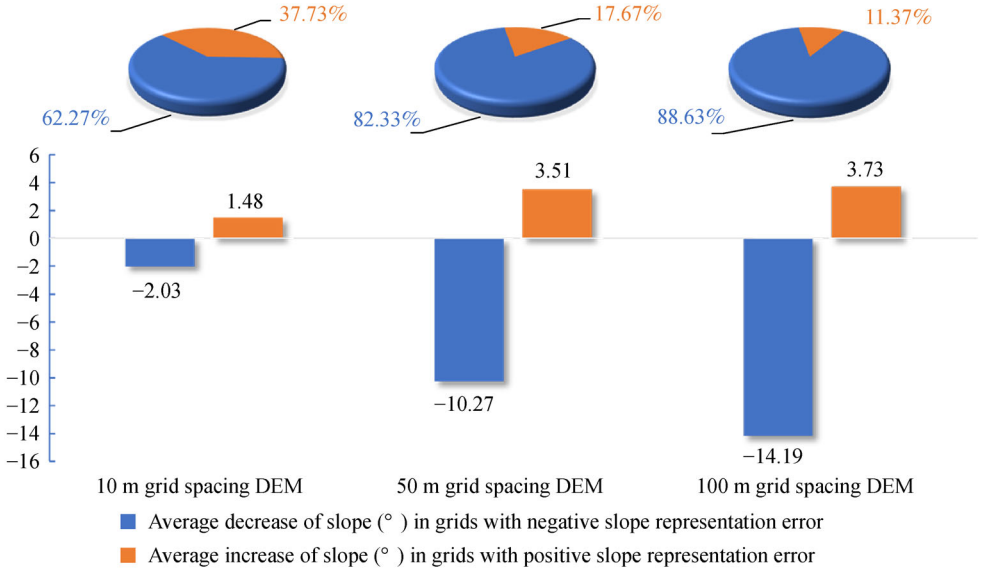

Fig. 6 Change in the slopes of grid cells with a positive or negative slope representation error in Nanping. The slope representation error is denoted by Slope_*RE*.

1) The figure shows that when the grid spacing of the digital elevation model (DEM) is 10 m, grid cells with a negative Slope_*RE* account for 62.24% of the total grid cells (see the blue section of the first pie chart on the left), and grid cells with a positive Slope_*RE* account for 37.71% of the total grid cells (see the orange section of the first pie chart on the left). We find that the ratio of the first percentage to the second is 62.24%/37.71%≈1.65>1. In a similar manner, we find that the corresponding ratio is approximately 4.66 (7.80) when the grid spacing is 50 (100) m, in this figure. Thus, the ratio increases (from 1.65 to 4.66 and then from 4.66 to 7.80) with the grid spacing. More generally, the corresponding ratio is greater than 1, ranging from 1.216 to 9.136, and increases with the grid spacing in all the sample areas. Note that the percentage of grid cells with a zero Slope_*RE* ranges from 0.00% to 2.89% in all the sample areas; thus, the grids with a zero Slope_*RE* are not discussed in this figure. 2) This figure shows that when the grid spacing is 10 m, the average decrease in slope is –2.03° (see the first blue bar from the left; the negative sign of –2.03° means that the slope decreases) in grid cells with a negative Slope_*RE*, and the average increase in slope is 1.48° (see the first orange bar from the left) in grid cells with a positive Slope_*RE*. Because |-2.03°|>|1.48°|, the average decrease is greater than the average increase, and the ratio of the former to the latter is 2.03°/1.48°≈1.37>1. In a similar manner, we find that the corresponding ratio is approximately 2.93 (3.80) when the grid spacing is 50 (100) m. Thus, the ratio increases (from 1.37 to 2.93 and then from 2.93 to 3.80) with the grid spacing. More generally, the corresponding ratio in all sample areas is greater than 1, ranging from 1.32 to 5.01, and the corresponding ratio increases with the grid spacing.

3.2 Change in positive, negative, or zero *SESR_RE* with grid spacing of the DEM

In Section 3.1, the grids are divided into three classes when the grid spacing changes. In this section, we discuss which classes of grids dominate the change in SESR.

Result 3. When the grid spacing of a DEM becomes coarser, the SESR generally increases on the grids with a negative Slope_*RE*.

We now explain Result 3 using the following data: We find that 2732914 grids have a negative Slope_*RE* when the grid spacing is 10 m in Nanping on the vernal equinox. Of the 2732914 grids, 2135772 grids (a percentage of 2135772/2732914≈78.15%) contribute to increases in the SESR (i.e., 2135772 grids have a positive *SESR_RE*). More generally, the corresponding percentages range from 50.15% to 95.10% in all the sample areas on the four selected days.

We now explain the reason for Result 3: First, we assume that when a grid has a negative Slope_*RE*, it may mainly be surrounded by grids with a negative Slope_*RE*. This assumption could be explained by an example related to grid *A* (see grid *A* in Fig. 5). Suppose that *A* has a negative Slope_*RE*. Then, by this assumption, the surrounding grids around *A* (see the 24 grids surrounding *A* in Fig. 5) may mainly have a negative Slope_*RE* (i.e., the slope decreases in most surrounding grids). This assumption has been confirmed (see Appendix A).

The reason for Result 3 may be as follows. When the slope in most surrounding grids decreases (see the assumption just mentioned), the represented relief decreases in these grids, reducing the shielding on *A* (see Fig. 5) caused by most of the surrounding grids (i.e., *A* may receive more sunshine and, thus, the PSD in *A* may increase, resulting in an increase in the SESR on *A*).

Then, we confirm the reason for Result 3. We find that in the grids with a negative Slope_*RE*, the shielding coefficients, PSD and SESR generally increase, with their average increases ranging from 0.02 to 0.36, 0.02 to 1.58 h and 0.05 to 6.61 MJ/m^2, respectively, in all sample areas on the four selected days. Then, the reason for Result 3 has been confirmed. In addition, we find Result 4.

Result 4. When the grid spacing of a DEM becomes coarser, the SESR generally decreases on the grids with a positive Slope_*RE*.

Specifically, the percentage of grids where the SESR decreases (*SESR_RE* is negative) and Slope_*RE* is positive compared to grids where Slope_*RE* is positive is from 51.67% to 89.14% in all sample areas on the four selected days. We may explain the reason for Result 4 in a similar way that we do for Result 3.

Result 5. When the grid spacing of a DEM becomes coarser, the grids with a negative Slope_*RE* dominate the increase in SESR (or average SESR).

Result 5 is explained by Fig. 7. By combining Results 1 through 4, we can explain the reason for Result 5. In addition, by combining Results 3 through 5, we may explain the reason for Result 6.

Result 6. The average SESR increases when the grid spacing of a DEM becomes coarser.

The significance of Results 3 through 6 may be as follows. The slope derived from the DEM changes with the grid spacing, resulting in a significant change in the SESR (Ruiz-Arias et al., 2009; Zhang et al., 2013), can be thoroughly explained on the grid level by using Results 3 through 5. By Result 6, we could expect a positive relation between the average SESR and the grid spacing and then give a more thorough understanding to the fact that the grid spacing positively influences the SESR (Zhang et al., 2010). We, however, fail to find the relation between *SESR_RE* and Aspect_*RE*.

A discussion about Result 6 is as follows. Suppose that theoretically, we have a DEM (named DEM A) with an infinitely fine grid spacing (although an infinitely fine grid spacing does not exist in practice) that perfectly represents a land surface. DEM A may yield the real SESR on the land surface. Suppose that a DEM in practice (named DEM B) also represents the land surface. Because the grid spacing of DEM B is always more than that of DEM A, the average SESR computed from DEM B is always more than that computed from DEM A, according to Result 6. Then, broadly speaking, any DEM in practice could yield the SESR whose average is always greater than the average of the corresponding real SESR. The discussion may be meaningful in practice.

The result that any DEM in practice could yield the SESR whose average is always greater than the average of the corresponding real SESR was tested in an indirect way in a test area which covers the latitudes from 27°14′10″ N to 27°14′32″ N and longitudes from 119°54′56″ E to 119°56′10″ E and with an approximate area of 2.288 km^2. We obtained the 0.5 m grid spacing DEM of the test area which was regarded to represent the real land surface of the test area (the DEM with infinite fine grid spacing does not exist in practice) and 30 m grid spacing DEM of the test area. Then, we computed the SESRs on the four selected days by using the two DEMs. The corresponding average values of the SESRs computed by the 0.5 m (30 m) grid spacing DEM were 33.35 (34.74) MJ/m^2 on the vernal equinox, 33.54 (34.81) MJ/m^2 on the summer solstice, 32.87 (34.26) MJ/m^2 on the autumnal equinox and 26.47 (27.72) MJ/m^2 on the winter solstice, respectively. The average value of SESR increased with the grid spacing of DEM. Thus, we have verified the result in an indirect way.

3.3 Relations between the error indexes of *SESR_RE* and Slope_*RE* or Aspect_*RE*

Result 7. There are positive relations of *SESR_AA* or *SESR_MSE* with Slope_*AA* or Slope_*MSE*, respectively; there are positive relations of *SESR_AA* or *SESR_MSE* with Aspect_*AA* or Aspect_*MSE*, respectively.

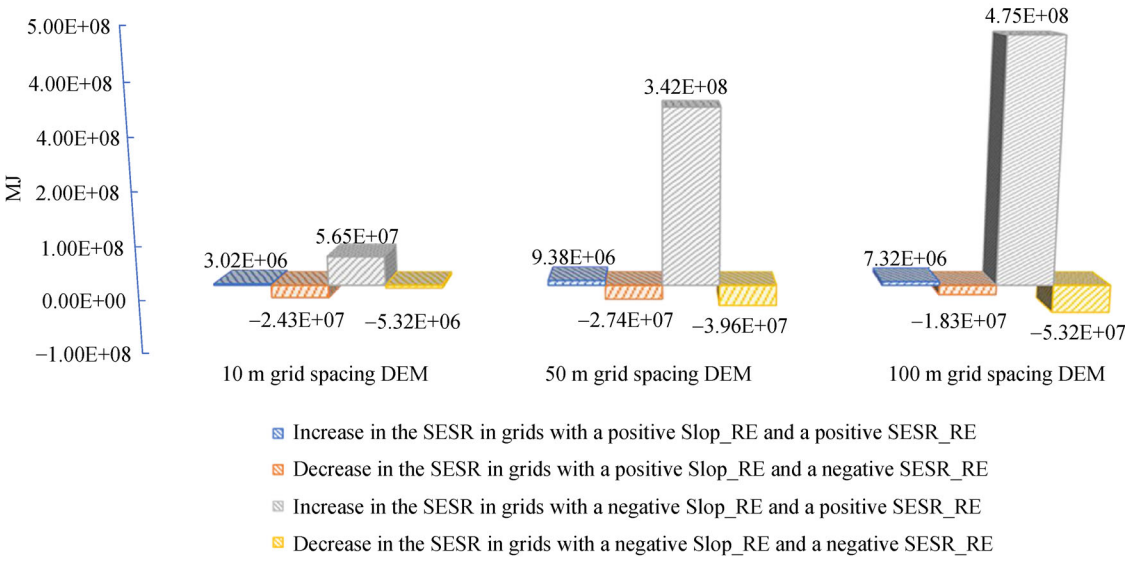

Fig. 7 Change in the *SESR* (shielded extra-terrestrial solar radiation) in grid cells with a positive or negative Slope_*RE* (slope representation error) in Nanping on the vernal equinox. The *SESR* representation error is denoted by *SESR_RE* in this figure.
This figure shows that when the grid spacing of the digital elevation model (DEM) is 10 m, the grid cells with a negative Slope_*RE* contribute a total increase in the *SESR* of −5.32E + 06 + 5.65E + 07≈5.12E + 07 MJ (see 5.65E + 07 and −5.32E + 06 in the third and fourth boxes from the left, respectively; the negative sign of −5.32E + 06 means that the *SESR* decreases), and grid cells with a positive Slope_*RE* contribute a total decrease in the *SESR* of −2.43E + 07 + 3.02E + 06≈−2.13E + 07 MJ (see −2.43E + 07 and 3.02E + 06 in the second and left boxes, respectively). Because the difference of −2.13E + 07 + 5.12E + 07≈2.99E + 07 MJ, the *SESR* should increase by approximately 2.99E + 07 MJ. Similarly, this figure shows that the corresponding difference is 2.84E + 08 (4.11E + 08) MJ when the grid spacing is 50 (100) m. Thus, the corresponding difference increases (from 2.99E + 07 to 2.84E + 08 then from 2.84E + 08 to 4.11E + 08 MJ) with the grid spacing. More generally, on the four selected days (the vernal equinox, summer solstice, autumnal equinox and winter solstice) in all the sample areas, the corresponding difference ranges from 1.51E + 06 to 5.63E + 08 MJ and increases with the grid spacing. Thus, grid cells with a negative Slope_*RE* dominate the increase in the *SESR* (or the increase in the average *SESR*) when the grid spacing becomes coarser in all the sample areas on the four selected days. In addition, we find that the grid cells with a zero Slope_*RE* do not contribute to any obvious change in *SESR*; the ratio of the change in *SESR* contributed by the grid cells with a zero Slope_*RE* to that contributed by the grid cells with a nonzero Slope_*RE* ranges from 3.01E-5 to 2.97E-4. The change is not illustrated in the figure for brevity.

The positive relations stated in Result 7 are found in each sample area on each of the four days and are described by Eqs. (5), (6), (7) and (8).

$$SESR_i\_AA = a_1 \times \text{slope}_i\_AA + b_1, \quad (5)$$

$$SESR_i\_MSE = a_2 \times \text{slope}_i\_MSE + b_2, \quad (6)$$

$$SESR_i\_AA = a_3 \times \text{aspect}_i\_AA + b_3, \quad (7)$$

$$SESR_i\_MSE = a_4 \times \text{aspect}_i\_MSE + b_4, \quad (8)$$

In Eqs. (5), (6), (7) and (8), a_k and b_k $(k = 1, 2, 3, 4)$ are parameters. The four equations are confirmed by a significance test with a confidence level of 0.05. a_k and b_k are given in Table 2. Note that in the four equations, a_k is positive.

We explain the reason for the positive relations described by Eqs. (5) and (6). When the grid spacing of the DEM becomes coarser, the difference between the surface represented by the DEM and the real surface may increase, resulting in a higher Slope_*RE* (i.e., Slope_*AA* or Slope_*MSE* may increase, which means a positive relation between the grid spacing and Slope_*AA* or Slope_*MSE*). The positive relation just mentioned can be confirmed by the coefficients between the grid spacing and Slope_*AA* (Slope_*MSE*), which range from 0.922 to 0.985 (0.877 to 0.977) in all the sample areas.

Similarly, we may explain the reason for the positive relations described by Eqs. (7) and (8). When the grid spacing of the DEM becomes coarser, the difference between the surface represented by the DEM and the real surface may increase, resulting in a higher Aspect_*RE* (i.e., Aspect_*AA* or Aspect_*MSE* may increase, which means a positive relation between the grid spacing and Aspect_*AA* or Aspect_*MSE*). The positive relation just mentioned could be confirmed by the coefficients between the grid spacing and Aspect_*AA* (Aspect_*MSE*), which range from 0.949 to 0.993 (0.928 to 0.990) in all the sample areas.

Based on Result 6, the increase in the average SESR with the grid spacing of a DEM may mean a larger SESR representation error. Then, we may expect a positive relation between the grid spacing and *SESR_AA* (*SESR_MSE*). The positive relation just mentioned could be confirmed by the corresponding coefficients, which range from 0.870 to 0.984 (0.835 to 0.977) in all the sample areas on the four selected days.

Generalizing the discussion above, we may explain the

Table 2 The parameters in Eqs. (5) through (8)

Sample area	Day	a_1	a_2	a_3	a_4	b_1	b_2	b_3	b_4
Nanping	Vernal equinox	21.61	23.90	9.94	10.30	0.29	0.48	0.63	0.74
	Summer solstice	20.48	22.66	9.42	9.76	0.32	0.48	0.65	0.72
	Autumnal equinox	21.23	23.50	9.76	10.13	0.28	0.48	0.62	0.73
	Winter solstice	29.98	30.91	13.80	13.32	0.18	0.37	0.66	0.70
Shenmu	Vernal equinox	21.75	22.19	3.96	5.00	0.03	0.18	0.33	0.52
	Summer solstice	9.84	13.85	1.78	3.09	0.15	0.41	0.30	0.64
	Autumnal equinox	21.32	21.79	3.89	4.91	0.03	0.18	0.32	0.52
	Winter solstice	29.63	27.35	5.41	6.17	−0.01	0.13	0.39	0.55
Sanming	Vernal equinox	18.15	21.54	8.34	9.47	0.42	0.53	1.03	1.03
	Summer solstice	17.08	19.20	7.84	8.41	0.54	0.79	1.12	1.25
	Autumnal equinox	17.82	21.17	8.19	9.30	0.42	0.53	1.01	1.02
	Winter solstice	26.10	28.46	12.03	12.56	0.21	0.29	1.07	0.92
Yanchuan	Vernal equinox	21.89	24.64	13.48	14.64	1.03	1.67	1.12	1.42
	Summer solstice	19.87	22.94	12.23	13.63	0.77	1.16	0.86	0.93
	Autumnal equinox	21.53	24.25	13.26	14.41	1.01	1.64	1.10	1.40
	Winter solstice	22.83	23.39	14.03	13.88	0.27	0.67	0.37	0.45
Yijun	Vernal equinox	21.80	23.57	10.16	12.53	0.48	1.22	0.73	1.26
	Summer solstice	17.64	21.65	8.22	11.51	0.49	1.04	0.69	1.07
	Autumnal equinox	21.43	23.20	9.99	12.33	0.48	1.21	0.72	1.24
	Winter solstice	22.08	21.09	10.31	11.22	0.06	0.53	0.31	0.56
Zhangzhou	Vernal equinox	12.03	12.68	1.38	2.27	0.02	0.09	−0.02	−0.36
	Summer solstice	8.12	10.65	0.93	1.90	0.04	0.11	0.01	−0.27
	Autumnal equinox	11.73	12.39	1.34	2.22	0.02	0.09	−0.02	−0.35
	Winter solstice	24.33	23.52	2.79	4.23	0.01	0.07	−0.08	−0.78

reason for the positive relations described by Eqs. (5) and (6), (7) and (8).

To verify the reliability of Eqs. (5), (6), (7) and (8), we conduct an experiment in the test area. Considering that of the six sample areas, Nanping is the one located nearest to the test area (the distance between Nanping and the test area is approximately 104 km), we may compute the *SESR_AA* in the test area by substituting the a_k and b_k values obtained in Nanping (given in Table 2) and the Slope_*AA* value computed in the test area into Eq. (5). The technical framework for verifying Eq. (5) is given in Fig. 8.

The average relative error (ARE) of the *SESR_AA* computed by Eq. (5) is defined in Fig. 8 and ranges from 6.36% to 12.55% (see Table 3). Similarly, we verify Eqs. (6), (7) and (8) in the test area and compute the corresponding AREs, which range from 6.36% to 9.24%, 9.51% to 12.55% and 7.07% to 9.74%, respectively (see Table 3). Then, Eqs. (5), (6), (7) and (8) may be verified if the upper limit of the ARE is set to 12.55%.

The significance of Eq. (5) may be as follows. By Eq. (5), a_1 and b_1 in an area can be computed by the $SESR_i\_AA$ and Slope_i_AA, which are computed in a few grids of the DEM representing the area. Then, based on the computed values for a_1 and b_1, researchers and users are able to compute the $SESR_i\_AA$ on any other grids of the DEM via Slope_i_AA, which can be easily computed, without the complicated computation of the SESR. In addition, Eqs. (6), (7) and (8) have the same significance.

3.4 Change in positive or negative *SESR_RE* or Slope_*RE* with grid spacing of the DEM when the slope is classified

Considering that the slope is usually classified in practice, we study the change in positive or negative *SESR_RE* with the grid spacing of the DEM when the slope derived from a 5 m grid spacing DEM was classified into 11 intervals $([0°, 5°), [5°, 10°), [10°, 15°), ..., [45°, 50°), [50°, 90°])$ numbered from 1 to 11. Because the percentage of grids with a slope interval of $[50°, 90°]$ was less than 0.3% in all sample areas, we do not divide the interval $[50°, 90°]$ into subintervals.

We compute the percentages of the grids with a positive *SESR_RE* on every classified slope when the grid spacings are 10 m, 15 m, …, 100 m (see Fig. 9).

Figure 9 shows that although the grid spacing changes, the distribution of the percentages on the classified slope

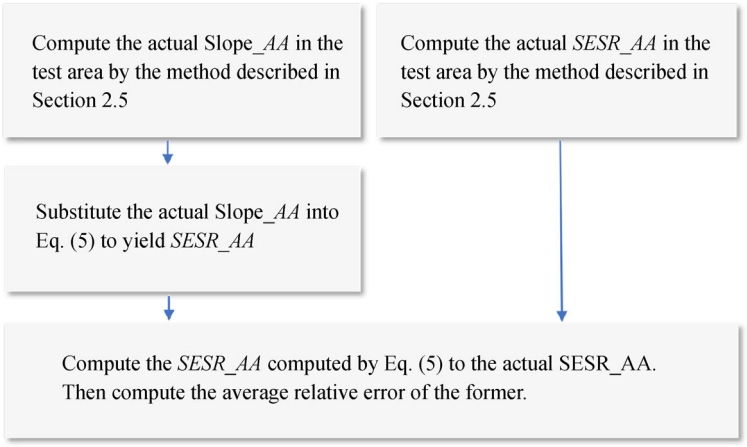

Fig. 8 Technical framework for verifying Eq. (5) in the test area. *SESR_AA* denotes the average absolute value of the slope representation error, and *SESR_AA* denotes the average absolute value of the shielded extra-terrestrial solar radiation. Equation (5) is given in Section 3.3. We compute the difference between the *SESR_AA* computed by Eq. (5) and the actual *SESR_AA*. Then, we define the ratio of the absolute value of the difference to the actual *SESR_AA* as the relative error of *SESR_AA* computed by Eq. (5). The average value of the relative error is defined as the average relative error of *SESR_AA* computed by Eq. (5).

Table 3 The average relative errors of *SESR_AA* and *SESR_MSE* in the test area*

ARE	Vernal equinox	Summer solstice	Autumnal equinox	Winter solstice
ARE of *SESR_AA* computed by Eq. (5)	10.70%	11.56%	10.72%	8.31%
ARE of *SESR_MSE* computed by Eq. (6)	8.85%	9.24%	8.86%	6.36%
ARE of *SESR_AA* computed by Eq. (7)	11.75%	12.55%	11.76%	9.51%
ARE of *SESR_MSE* computed by Eq. (8)	9.26%	9.74%	9.27%	7.07%

Note: *The average relative error (ARE) is defined in Fig. 8.

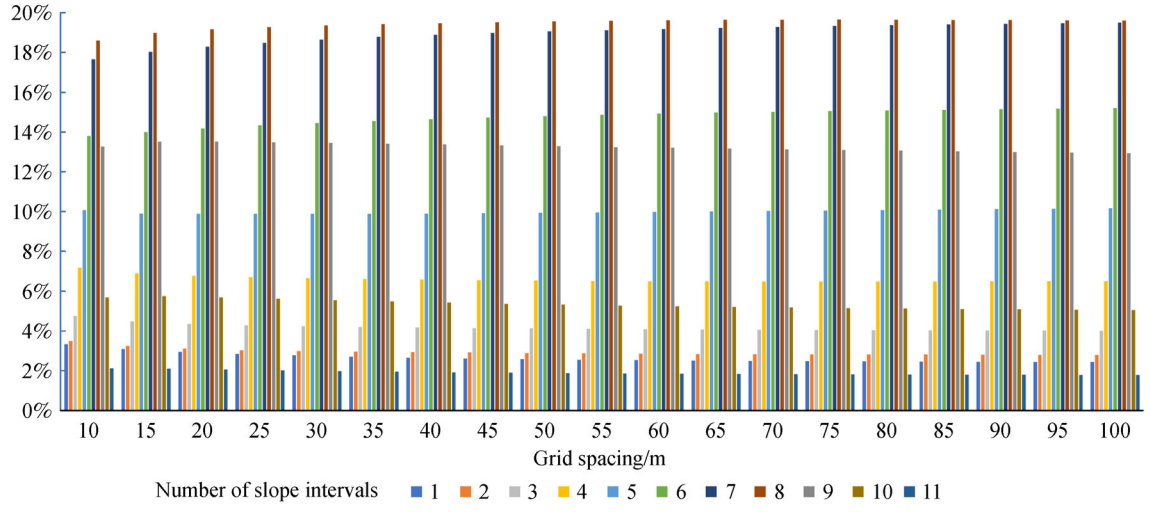

Fig. 9 Percentage of grid cells with a positive representation error of the shield extra-terrestrial solar radiation, denoted by *SESR_RE*, in Nanping on every classified slope on the vernal equinox. The shielded extra-terrestrial solar radiation is computed from digital elevation models (DEMs) with grid spacings of 10 m, 15 m, …, 100 m. The slope derived from the DEM with 5 m grid spacing is classified into 11 intervals, [0°, 5°), [5°, 10°), [10°, 15°), ..., [45°, 50°),[50°, 90°], numbered from 1 to 11. The percentages of grid cells with a positive or negative *SESR_RE* in other sample areas are not given here because of lack of space.

fail to change in terms of statistics — we perform a one-way analysis of variance with a null hypothesis that the distributions of the percentages of different grid spacings are from the same distribution; we find that all corresponding p-values are 1.000, and the null hypothesis cannot be rejected. Similarly, we find that the distribution of the percentages of grids with a negative *SESR_RE* on every classified slope fail to change in terms of statistics though the grid spacing changes — all the corresponding p-values are 1.000. These findings can be expressed in Result 8.

Result 8. Based on statistics, the distribution of the percentage of grids with a positive *SESR_RE* or a negative *SESR_RE* on the classified slope is independent of the grid spacing of the DEM.

We explain the reason for Result 8. First, the distribution of the percentage of grids with a positive (or negative) Slope_*RE* on the classified slope is independent of the grid spacing of the DEM (Chen, 2014). Second, based on Result 3 and Result 4, a positive *SESR_RE* generally appears on grids with a negative Slope_*RE*, and vice versa. Together, the independence of the distribution of a positive or negative Slope_*RE* on the classified slope may be extended to the distribution of a negative or positive *SESR_RE*.

In addition, Fig. 9 shows that the distribution of the percentages of positive *SESR_RE* values are concentrated on the slope intervals numbered from 5 to 9 (i.e., the majority is found in this concentration). The corresponding concentrations of positive or negative *SESR_RE* values on the corresponding slope intervals are found in all sample areas on the four selected days. The findings mentioned above may be caused by the following reasons:

When the grid spacing of a DEM becomes coarser, whether the slope of a land surface derived from the DEM increases or decreases is determined by the first-order and third-order derivative (or partial derivative) of the function that describes the land surface (Chen, 2013). In other words, the function describing the geometrical feature of the land surface determines whether the slope increases or decreases (i.e., whether Slope_*RE* is positive or negative). Whether Slope_*RE* is positive or negative generally determines whether *SESR_RE* on the land surface is negative or positive (based on Result 3 and Result 4, respectively). Then, whether *SESR_RE* is negative or positive may be generally determined by the geometrical feature of the land surface whose slope derived from the 5 m grid spacing DEM is a certain value, resulting in a relation between the slope and the sign of *SESR_RE*. Based on the relation, we may explain the concentration of the positive or negative *SESR_RE* values within the corresponding slope intervals.

3.5 Distribution of the values of *SESR_AA* (or *SESR_MSE*) on the classified slope

We analyze the *SESR_AA* (or *SESR_MSE*) for the 11 intervals and find Result 9.

Result 9. The *SESR_AA* (or *SESR_MSE*) generally increases when the number of slope intervals increases from 1 to 11.

As shown in Fig. 10, *SESR_AA* generally increases when the number of slope intervals increases from 1 to 11 (i.e., the slope increases in all the sample areas on the four selected days). In addition, as shown in Fig. 11, the *SESR_MSE* generally increases when the number of slope intervals increases from 1 to 11 in all sample areas on the

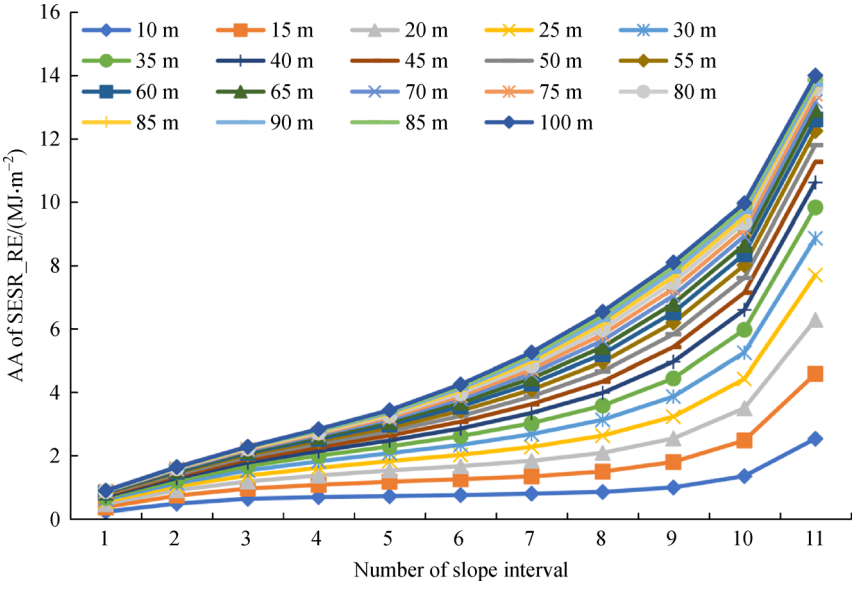

Fig. 10 Average absolute value of the shielded extra-terrestrial solar radiation representation error (i.e., the AA of SESR_RE) distributed across the 11 slope intervals of [0°, 5°), [5°, 10°), [10°, 15°), ..., [45°, 50°),[50°, 90°]. The shielded extra-terrestrial solar radiation is computed from digital elevation models with grid spacings of 10 m, 15 m, …, 100 m in Nanping on the vernal equinox.

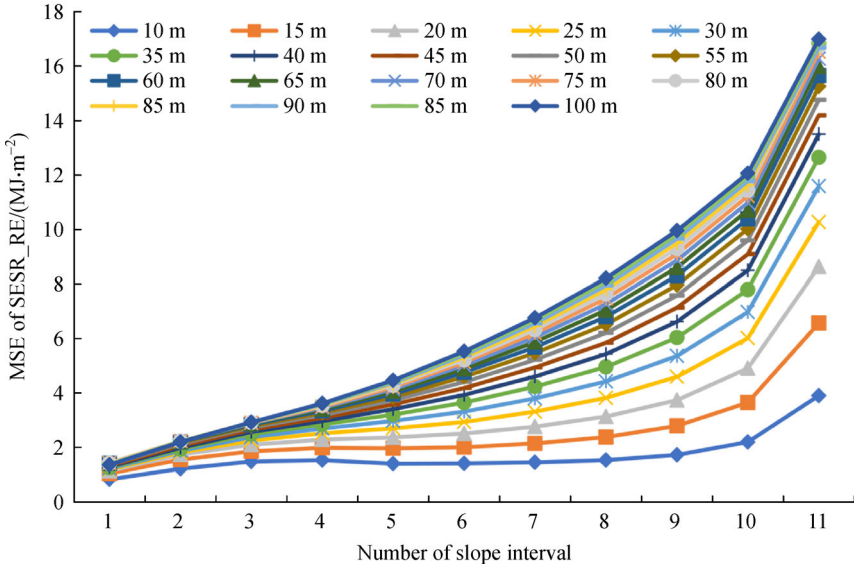

Fig. 11 Mean square errors of shielded extra-terrestrial solar radiation representation error (i.e., the MSEs of SESR_RE) distributed across the 11 slope intervals of [0°, 5°), [5°, 10°), [10°, 15°), ..., [45°, 50°),[50°, 90°]. The shielded extra-terrestrial solar radiation is computed from digital elevation models with grid spacings of 10 m, 15 m, …, 100 m in Nanping on the vernal equinox.

four selected days.

We explain the reason for Result 9 by using the following two results.

Slope_*AA* (or Slope_*MSE*) generally increases when the number of slope intervals increases in all the sample areas on the four selected days, as shown in Fig. 12 (Fig. 12 shows Slope_*AA* on the 11 intervals only in Nanping for brevity).

A positive relation between Slope_*AA* (Slope_*MSE*) and *SESR_AA* (*SESR_MSE*) in Result 7 still exists when the slope is classified into 11 intervals (when the slope is classified, the correlation coefficients between the Slope_*AA* and *SESR_AA* range from 0.805 to 1.000 in all sample areas on the four selected days).

By combining the two results, we conclude that *SESR_AA* or *SESR_MSE* generally increase when the number of slope intervals increases.

Based on Result 9, we may more deeply understand that "the slope has a positive relation with solar radiation" (Hang et al., 2010).

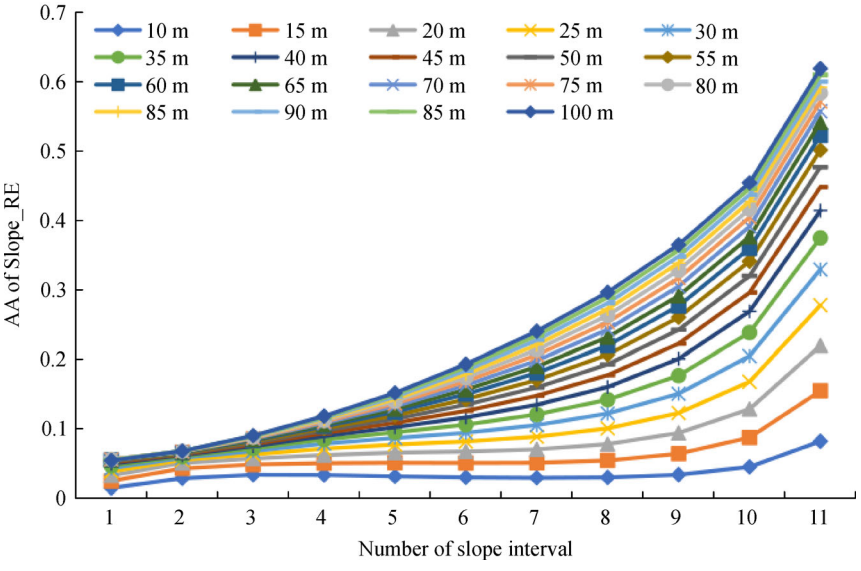

Fig. 12 Average absolute value of the slope representation error (i.e., the AA of Slope_*RE*) (in radians) for the 11 slope intervals of [0°, 5°), [5°, 10°), [10°, 15°), ..., [45°, 50°),[50°, 90°]. The slope representation error is computed from digital elevation models with grid spacings of 10 m, 15 m, …, 100 m in Nanping.

3.6 Discussion on the influence of the locations of the sample areas on Results 3, 4, 6, 7, 8 and 9

The computation of SESR reveals that the locations of the sample areas (in the Northern or Southern Hemisphere) and the landforms of the sample areas could influence Results 3, 4, 6, 7, 8, and 9.

We have compared the results of the sample areas that are classified by landforms and fail to find any obvious pattern related to the landforms, though we could study the SESR under the diversified possibilities based on whether the grids in the DEMs of the sample areas face into or away from the sun during a day (see Fig. 13). This failure may be caused by two reasons. First, the number of sample areas may be insufficient; second, we do not have sample areas at the same latitude representing various landforms. This assessment should be performed in future work. In addition, this failure means that we may study the influence of the locations of the sample areas, avoiding the influence of the landforms of the sample areas.

We now discuss how the locations of the sample areas influence Results 3, 4, 6, 7, 8, and 9. Suppose that the six sample areas are moved to the equator (0°), to the latitude of 20°S and to the latitude of 40°S (we do not discuss the change in the SESR during the polar day and the polar night, so the sample areas are not moved to 80°S where the polar day and polar night occur; considering that the southeast point of the continent of South American does not touch 60°S or a higher latitude than 60°S, we do not move the sample areas to 60°S). Then, we compute the corresponding SESRs in the sample areas at the given latitudes. When analyzing the SESRs, we could decide how the locations of the sample areas influence Results 3, 4, 6, 7, 8, and 9 without considering the influence of the landforms of the sample areas.

Discussion on Result 3. Let Nanping be moved to the equator. When the grid spacing is 10 m (50 m), approximately 91.13% (92.23%) of the grid with a negative Slope_*RE* contribute to the increase in the SESR in Nanping on the vernal equinox. More generally, the corresponding percentage ranges from 51.03% to 97.06% in all the sample areas on the four selected days when the sample areas are moved to latitudes of 0°, 20°S and 40°S. Then, Result 3 is confirmed at latitudes of 0°, 20°S and 40°S.

Discussion on Result 4. Let Nanping be moved to the equator. The percentage of grids where the SESR decreases (*SESR_RE* is negative) and Slope_*RE* is positive compared to grids where Slope_*RE* is negative ranges from 75.66% to 85.54% in Nanping on the vernal equinox. The corresponding percentages in all the sample areas on the four selected days are more than 50.00% (when the sample areas are moved to latitudes of 0°, 20°S and 40°S) but under a few conditions, e.g., when Zhangzhou is moved to 40°S and the grid spacing is more than 25 m, the corresponding percentages range from 48.14% to 49.67% on the summer solstice (however, the number of the grids with a negative Slope_*RE* and positive *SESR_RE* is more than that of the grids with a positive Slope_*RE* and negative *SESR_RE* under this condition. The ratio of the first number to the latter number is 1.45 to 3.22; the ratio of the corresponding mean increase in SESR to the corresponding mean decrease in SESR is 1.61 to 2.76 under this condition. Then, the SESR has to also increase with the grid spacing under this condition.). Together, we may state that generally, SESR decreases in the grids with positive Slope_*RE*.

Discussion on Result 6. Let Nanping be moved to the equator. The average SESR in Nanping on the vernal equinox increases with the grid spacing, e.g., the average SESR is 31.37 MJ·m^{-2}, 34.19 MJ·m^{-2} and 35.39 MJ·m^{-2} when the grid spacing is 5 m, 50 m and 100 m, respectively (see Fig. 14). More generally, the average SESR increases with the grid spacing in all the sample areas on the four selected days when the sample areas are moved to latitudes of 0°, 20°S and 40°S.

Discussion on Result 7. We find the positive relations described by Eqs. (5), (6), (7) and (8) in all the sample

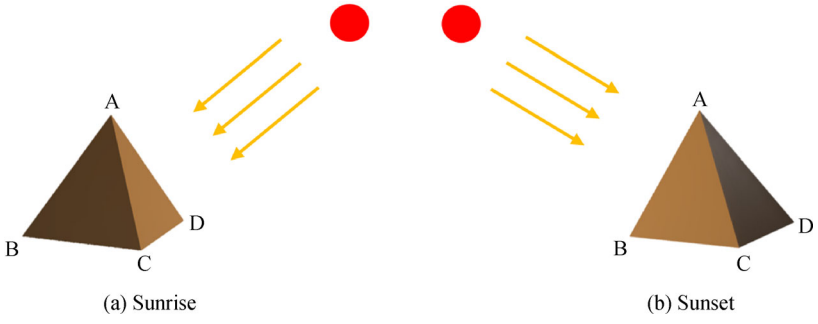

Fig. 13 Side facing into or away from the sun. In the figure on the left, (a) Sunrise, face ACD of pyramid ABCD faces into the sun (represented by the red disk), at sunrise, while face ABC faces away the sun. In the figure on the right, (b) Sunset, face ACD faces away the sun, while face ABC faces into the sun. Then, although the aspect of ACD or ABC is certain, whether ACD or ABC faces into or away the sun varies with time. Furthermore, because all the grid cells in the DEMs of the sample areas possess diversified slopes and aspects, the grid cells may have diversified possibilities on whether they face into or away from the sun during the day, making it possible for us to study the shielded extra-terrestrial solar radiation under diversified possibilities.

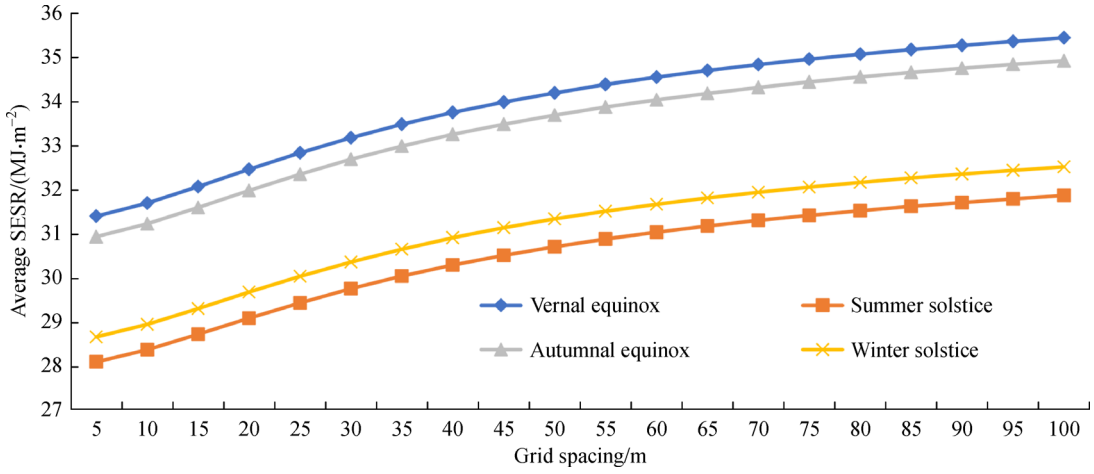

Fig. 14 The average shielded extra-terrestrial solar radiation (SESR) in Nanping moved to the equator on the vernal equinox, summer solstice, autumnal equinox and winter solstice when the grid spacings of the digital elevation model are 5, 10, ..., 100 m.

areas on the four selected days when they are moved to 0° or 20°S or 40°S. The four equations are confirmed by a significance test with a confidence level of 0.05. Note that in the four equations, a_k is positive (the minimum a_k is approximately 0.54). The a_k and b_k are not given here for brevity; we obtain 72 sets of a_1 and b_1 ($72 = 6 \times 4 \times 3$, with 6 representing the six sample areas, 4 representing the four selected days and 3 representing the three latitudes) and 72 sets of a_2 and b_2, 72 sets of a_3 and b_3 and 72 sets of a_4 and b_4.

Discussion on Result 8. We perform a one-way analysis of variance with a null hypothesis that the distributions of the percentages of grids with a positive *SESR_RE* on every classified slope are from the same distribution; we find that all corresponding p-values are 1.000, and the null hypothesis cannot be rejected. Similarly, we find that the distribution of the percentages of grids with a negative *SESR_RE* on every classified slope fails to change in terms of statistics though the grid spacing changes — all the corresponding *p*-values are 1.000.

Discussion on Result 9. When the number of slope intervals increases from 1 to 11, the *SESR_AA* (*SESR_MSE*) increases or has an upward trend under a few conditions if all sample areas are moved to 0° or 20°S or 40°S.

We fail to find any fundamental changes to the Results 3, 4, 6, 7, 8 and 9 that are caused by the locations of the sample areas.

3.7 Limitations and applications of the findings in this study

3.7.1 Limitations of the findings in this study

Although aspect influences SESR (Zeng et al., 2005) (or solar radiation (Wang et al., 2014)), we find that the sign of Aspect_*RE* does not obviously relate to that of *SESR_RE*; we fail to find some obvious pattern in the distribution of the percentages of the *SESR_AA* or *SESR_MSE* on aspect which is classified into 9 classes (north, north-east, east, south-east, south, south-west, west, north-west and flat). We, however, fail to discover the reason explaining these results.

In this study, we do not consider how the errors in latitude and solar decline affect the SESR representation error, although latitude and solar decline are required variables for computing the SESR (see Eq. (1)). The corresponding affect could be studied in future work.

We do not discuss the change in the SESR during the polar day and polar night because the change may be quite complicated and could not be discussed thoroughly in this paper for lack of room. The corresponding discussion may be interesting and worth doing in the future.

3.7.2 Applications of the findings in this study

Applications of Eqs. (5), (6), (7), and (8). These four equations can be used to compute *SESR_AA* or *SESR_MSE*, both of which are not easily computed in practice because of the difficulty in obtaining the actual solar radiation or the SESR over a large region. This difficulty is generally caused by factors such as "the inappropriate density of stations" that survey solar radiation ("particularly in complex peripheral national territories") (Ambreen et al., 2011) and the lack of satisfactory sunshine hour data. We, however, can easily survey the actual slope or aspect and derive the slope or aspect from the DEM, by which we can compute Slope_*AA* and Slope_*MSE* (or Aspect_*AA* and Aspect_*MSE*). Then, we can compute *SESR_AA* or *SESR_MSE* using the corresponding equation from the four equations above.

Applications of the results (Results 1 through 9). These results may add to the current knowledge of how Slope_*RE* propagates toward *SESR_RE* and how to estimate *SESR_RE*. Then, when researchers conduct studies in

which the SESR is the data of interest, they may avoid incorrect results caused by the SESR representation error. Moreover, users who make important decisions using the SESR can avoid mistakes. Furthermore, this study might be beneficial for research in the fields of spatial data errors and digital terrain analysis. In addition, based on Result 9, the lower the slope on a grid is, the more reliable the SESR computed on the grid is. Then, the method for computing the SESR may be applied in regions with low slopes.

4 Conclusions

In this paper, we have defined a set of concepts and developed the corresponding methods to describe the representation errors in slope, aspect and SESR; the representation errors are unavoidable and useful for understanding how the SESR varies with the grid spacing of a DEM. The scale of DEM exerts an obvious influence on the computed slope and the SESR. We draw the following conclusions:

Let a surface be represented by a gridded DEM.

1) When the grid spacing of the DEM becomes coarser, the grids with a negative Slope_*RE* dominate the change in slope, resulting in a decrease in the average slope and an increase in the PSD and the SESR. When the grid spacing becomes coarser, the SESR generally increases in the grids with a negative Slope_*RE*, and vice versa. The DEM could yield the SESR whose average is generally greater than the average of the corresponding real SESR.

2) We may compute *SESR_AA* or *SESR_MSE* using Slope_*AA* or Slope_*MSE* (Aspect_*AA* or Aspect_*MSE*), respectively, in practice because the corresponding relations are sufficiently linear.

3) When the slope is classified into 11 intervals, *SESR_AA* or *SESR_MSE* increase with the number of intervals. The distribution of the percentages of positive *SESR_RE* values on the classified slope is independent of the grid spacings of the DEM and concentrates on some slope intervals.

4) The locations of the sample areas (in the Northern or Southern Hemisphere) fail to cause any essential changes to Results 3, 4, 6, 7, 8 and 9.

The results of this study may lead to fast forecasting of *SESR_RE* at a global level and may be beneficial to the development of the accuracy theory of spatial data, extending its application into studies on solar radiation and energy. In future work, we will study how the errors in latitude and solar declination propagate toward the SESR and discuss how seasons influence the relation between *SESR_AA* (*SESR_MSE*) and Slope_*AA* (Slope_*MSE*).

Acknowledgements This work is supported by the National Natural Science Foundation of China (Grant Nos. 41771423, 41930102, 41601408 and 41471331) and the Industry University Research Cooperation Project for the Social Development of Fujian Province, China (No. 2018Y0054). The author is thankful to the anonymous reviewers for their helpful comments; the author is indebeted to his students, Wenzhen Zhou, Huange LI, Quanjin LI and Tinmin Lin for retouching the figures.

References

Ambreen R, Qiu X F, Ahmad I (2011). Distributed modeling of extraterrestrial solar radiation over the rugged terrains of pakistan. J Mt Sci, 8(3): 427–436

Bocquet G (1984). Method of study and cartography of the potential sunny periods in mountainous areas. J Climatol, 4(6): 587–596

Chen N (2013). Influence of resolutions of DEM on the error of slope. Geomatics and Information Science of Wuhan University, 38(5): 594–598 (in Chinese)

Chen N (2014). Relationship between dem resolution and average slope derived from DEM. Journal of Geo-Information Science, 16(4): 524–530 (in Chinese)

Chen N, Tang G A, Guo D S, Chen C (2014). Influence of DEM orientation on the error of slope calculation. Earth Sci Inform, 7(4): 277–285

Chow T E, Hodgson M E (2009). Effects of lidar post—spacing and DEM resolution to mean slope estimation. Int J Geogr Inf Sci, 23(10): 1277–1295

Dozier J, Frew J (1990). Rapid calculation of terrain parameters for radiation modeling from digital elevation data. IEEE Trans Geosci Remote Sens, 28(5): 963–969

Gao J (1997). Resolution and accuracy of terrain representation by grid DEM s at a micro-scale. Int J Geogr Inf Sci, 11(2): 199–212

Gao J, Burt J E, Zhu A X (2012). Neighborhood size and spatial scale in raster-based slope calculations. Int J Geogr Inf Sci, 26(10): 1959–1978

Häntzschel J, Goldberg V, Bernhofer C (2005). GIS-based regionalisation of radiation, temperature and coupling measures in complex terrain for low mountain ranges. Meteorol Appl, 12(1): 33–42

Hopkinson C, Chasmer L, Munro S, Demuth M N (2010). The influence of DEM resolution on simulated solar radiation—induced glacier melt. Hydrol Processes, 24(6): 775–788

Horn B K P (1981). Hill shading and the reflectance map. Proc IEEE, 69 (1): 14–47

Huang W F, Chen M R, Chen S X (1986). Meteorology and Climatology. Beijing: Higher Education Press (in Chinese)

Li C, Wang Q, Shi W Z, Zhao S (2018a). Uncertainty modelling and analysis of volume calculations based on a regular grid digital elevation model (DEM). Comput Geosci, 114: 117–129

Li C, Zhao S S, Wang Q, Shi W (2018b). Uncertainty modeling and analysis of surface area calculation based on a regular grid digital elevation model (DEM). Int J Geogr Inf Sci, 32(9): 1–23

Li X, Cheng G, Chen X, Lu L (1999). Modification of solar radiation model over rugged terrain. Chin Sci Bull, 44(15): 1345–1349

Li Z Q, Weng D M (1988). A computer model for calculating the duration of sunshine in mountainous areas. Chin Sci Bull, 33(19): 1624–1627

Liu M, Bárdossy A, Jiang Y (2012). Gis-based modelling of topography-induced solar radiation variability in complex terrain for data sparse region. Int J of Geogr Inf Sci, 26(7): 1281–1308

Pellicciotti F, Raschle T, Huerlimann T, Carenzo M, Burlando P (2011). Transmission of solar radiation through clouds on melting glaciers: A comparison of parameterizations and their impact on melt modelling. J Glaciol, 57(202): 367–381

Piedallu C, Gégout J C (2007). Multiscale computation of solar radiation for predictive vegetation modelling. Ann Sci, 64(8): 899–909

Piedallu C, Gégout J C (2008). Efficient assessment of topographic solar radiation to improve plant distribution models. Agric Meteorol, 148 (11): 1696–1706

Qiu X F, Zeng Y, Liu C M, Wu X (2004). Simulation of astronomical solar radiation over yellow river basin based on DEM. J Geogr Sci, 14(1): 63–69

Qiu X F, Zeng Y, Liu S M (2005). Distributed modeling of extraterrestrial solar radiation over rugged terrain. Chin J Geophys, 48(5): 1100–1107

Reuter H I, Kersebaum K C, Wendroth O (2005). Modelling of solar radiation influenced by topographic shading—evaluation and application for precision farming. Phys Chem Earth Parts ABC, 30 (1–3): 143–149

Ruiz-Arias J A, Tovar-Pescador J, Pozo-Vázquez D, Alsamamra H, (2009). A comparative analysis of DEM-based models to estimate the solar radiation in mountainous terrain. Int J Geogr Inf Sci, 23(8): 1049–1076

Šúri M, Huld T A, Dunlop E D, Ossenbrink H A (2007). Potential of solar electricity generation in the european union member states and candidate countries. Sol Energy, 81(10): 1295–1305

Tang G A, Strobl J, Gong J Y, Zhao M D, Chen Z J (2001). Evaluation on the accuracy of digital elevation models. J Geogr Sci, 11(2): 209–216

Wang L, Qiu X F, Wang P, Wang X, Liu A (2014). Influence of complex topography on global solar radiation in the Yangtze River Basin. J Geogr Sci, 24(6): 980–992

Yao R M, Luo Q, Li B Z (2011). A simplified mathematical model for urban microclimate simulation. Build Environ, 46(1): 253–265

Zeng Y, Qiu X F, Liu C M, et al. (2005). Distributed modeling of direct solar radiation on rugged terrain of the Yellow River Basin. J Geogr Sci, 15(4): 439–447

Zeng Y, Qiu X F, Miao Q L, Liu C (2003). Distribution of possible sunshine durations over rugged terrains of China. Prog Nat Sci, 13 (10): 761–764

Zhang H L, Liu G H, Huang C (2010). Modeling all-sky global solar radiation using modis atmospheric products: a case study in Qinghai-Tibet Plateau. Chin Geogr Sci, 20(6): 513–521

Zhang H L, Xin X Z, Li L, Liu Q (2013). An improved parametric model for simulating cloudy sky daily direct solar radiation on tilted surfaces. IEEE J Sel Top Appl Earth Obs Remote Sens, 6(1): 180–187

Zhang J Y, Zhao L, Deng S, Xu W, Zhang Y (2017). A critical review of the models used to estimate solar radiation. Renew Sustain Energy Rev, 70: 314–329

Zhang S H, Li X G, Chen Y N (2015). Error assessment of grid-based direct solar radiation models. Int J Geogr Inf Sci, 29(10): 1782–1806

Zhang Y L, Li X, Bai Y L (2015). An integrated approach to estimate shortwave solar radiation on clear-sky days in rugged terrain using modis atmospheric products. Sol Energy, 113: 347–357

Zhou Q M, Liu X J (2002). Error assessment of grid-based flow routing algorithms used in hydrological models. Int J Geogr Inf Sci, 16(8): 819–842

Zhou Q M, Liu X J (2004). Analysis of errors of derived slope and aspect related to DEM data properties. Comput Geosci, 30(4): 369–378

Zhou Q M, Liu X J (2008). Assessing Uncertainties in Derived Slope and Aspect from a Grid DEM. Berlin: Springer, 279–306

Zuo D K (1990). Dictionary of Modern Geography. Beijing: The Commercial Press (in Chinese)

Zuo D K, Zhou Y H, Xiang Y Q, et al. (1991) Studies on Radiation in the Epigeosphere. Beijing: Science Press (in Chinese)

Appendix A

First, consider a 3 × 3 grid matrix that consists of one center grid and 8 other grids. If we define the center grid as being surrounded by the 8 other grids, we find that of the 8 surrounding grids, there is an average of 5.23 to 7.74 grids with a negative Slope_*RE* in all the sample areas. Note that 5.23/8>1/2, which means that the surrounding grids with a negative Slope_*RE* comprise the majority.

Second, consider a 5 × 5 grid matrix that consists of one center grid and 24 other grids. We find that of the 24 surrounding grids, there is an average of 13.97 to 22.96 grids with a negative Slope_*RE* in all the sample areas. Note that 13.97/24>1/2.

Third, consider a 7 × 7 grid matrix that consists of one center grid and 48 other grids. We find that of the 48 surrounding grids, there is an average of 27.15 to 45.51 grids with a negative Slope_*RE* in all the sample areas. Note that 27.15/48>1/2.

Fourth, consider a 9 × 9 grid matrix that consists of one center grid and 80 other grids. We find that of the 80 surrounding grids, there is an average of 44.63 to 75.34 grids with a negative Slope_*RE* in all the sample areas. Note that 44.63/80>1/2.

Due to a lack of space, we do not discuss grid matrixes larger than 9 × 9 in this paper.

Finally, the assumption may be confirmed.

Note that the confirmed assumption may reveal that the negative Slope_*RE* is spatially clustered, which might merit further investigation.